Volume 55
Number 7
17 February 2026
Pages 2731-3154

Dalton Transactions

An international journal of inorganic chemistry

rsc.li/dalton

ISSN 1477-9226

ROYAL SOCIETY OF CHEMISTRY

PAPER

Pablo J. Sanz Miguel *et al.*

Unveiling n → π* interactions: convergence of quantum crystallography and computational insights

Dalton Transactions

ROYAL SOCIETY OF CHEMISTRY

PAPER

View Article Online
View Journal | View Issue

Cite this: *Dalton Trans.*, 2026, **55**, 2825

Unveiling n → π* interactions: convergence of quantum crystallography and computational insights

Alvaro Polo, Pilar García-Orduña, Jorge Echeverría and Pablo J. Sanz Miguel *

Received 6th October 2025,
Accepted 19th December 2025

DOI: 10.1039/d5dt02386f

rsc.li/dalton

We report the identification and characterization of a n → π* interaction between halide anions and a cationic purine nucleobase. Through a combined quantum crystallographic and computational approach, we demonstrate that perpendicular anion···(sp^2)carbon contacts occur consistently at the C2 position of the purine nucleobase, with geometries and energies comparable to hydrogen bonds. High-resolution X-ray charge density analysis of **2**[Br]·H_2O confirms the existence of a bond path and an electron density depletion on C2, supporting a charge-transfer interaction. Complementary theoretical studies reveal a lone pair-to-π* orbital delocalization mechanism, with second-order NBO energies up to 6 kcal mol^{-1}. The interaction persists with various anions, hydration levels, and C2 substitutions, highlighting its robustness and potential relevance in supramolecular chemistry. This study provides the experimental validation of an n → π* contact, supported by topological and electrostatic descriptors.

Introduction

The existence of non-covalent lone-pair (n) to antibonding orbital (π*) interactions was first postulated decades ago in the context of DNA stabilization.[1] Since then, n → π* interactions have been recognized in several conformational processes, such as folding of peptides into triple helices[2] or the control of amide isomerism.[3] These examples have established the importance of n → π* interactions in the structural behavior of macromolecular biological systems, acting along with classical hydrogen bonds.[4,5]

At the molecular level, stabilizing n → π* interactions involve the delocalization of a lone-pair from a donor atom into an empty π* orbital on an acceptor moiety. These acceptors are usually aromatic rings or carbonyl groups,[6,7] provided that the interaction geometry allows for effective orbital overlap. While usually considered weaker than hydrogen or halogen bonds,[8] such contacts can influence molecular conformation and packing. In carbonyl systems, computational studies have shown that the stabilization arises from the combination of charge transfer due to orbital overlap and electrostatic attractions between the electron-rich lone pair and the electron density depleted region of the carbonyl associated with a π-hole.[9,10]

A related class of interactions, anion···π contacts, have been extensively studied in recent years. Since their first description[11] which was followed by some controversy,[12] these interactions between anions and electron-deficient π-systems have now been observed in a wide variety of contexts, including supramolecular assemblies,[13,14] catalysis,[15] and biomolecular recognition.[16] These contacts often involve aromatic systems exhibiting electropositive π-surfaces and are typically probed *via* a combination of experimental and theoretical approaches.

Experimentally, anion···π interactions are usually characterized by X-ray crystallography and NMR spectroscopy, which reveal structural motifs, distances, and angles.[17] Analysis often relies on deviations from van der Waals distances, despite the known challenges when dealing with ionic radii.[18,19] On the theoretical side, density functional theory (DFT) provides insights into interaction energies, preferred geometries, and electrostatic features such as molecular quadrupole moments and electrostatic potentials.[11,17] Furthermore, Quantum Theory of Atoms in Molecules (QTAIM)[20] offers topological descriptors (bond paths, electron density, Laplacians, *etc.*) that help rationalize the weak anion···π contacts.

Notably, this topological approach can also be applied to experimental charge densities derived from high-resolution crystallography, as demonstrated in the study of iodide···quinoid interactions.[7] Although its application is challenging if heavy atoms are involved, this approach remains a robust and experimentally supported method to evaluate weak intermolecular interactions.

In this work, we combine experimental and theoretical methodologies to investigate n → π* interactions between

Departamento de Química Inorgánica, Instituto de Síntesis Química y Catálisis Homogénea (ISQCH), Universidad de Zaragoza-CSIC, 50009 Zaragoza, Spain. E-mail: pablo.sanz@unizar.es

halide anions and a positively charged purine nucleobase. These short X···C2 contacts (X = halide), oriented nearly perpendicular to the aromatic plane, are consistently observed across a family of hypoxanthinium salts with varying halides, hydration levels, and ring substitution patterns. Indeed, protonation of nucleobases has been postulated as a scenario where significant n → π* binding energies are expected to arise, due to the positive polarization of the rings.[21] We selected the hypoxanthine scaffold as a model due to its chemical tunability and biological relevance. Our study reveals a consistent, measurable n → π* interaction that is energetically comparable to hydrogen bonding, validated by high-resolution X-ray diffraction (quantum crystallography), experimental electron density topological analysis, and DFT-based modeling.

Results and discussion

Nearly a century ago, Biltz and Rakett reported the synthesis of caffeidinium nitrate, **1**[NO_3], upon decarboxylation of caffeine in alkaline medium followed by precipitation with nitric acid (Scheme 1).[22] Further deprotonation of **1**[NO_3] leads to the isolation of caffeidine,[23] which upon reprotonation with HCl, in a subsequent step, yields **1**[Cl] (SI).

Using single crystal X-ray diffraction analysis,[24–28] we structurally characterized both salts, namely, **1**[NO_3] and **1**[Cl].[29] In both cases, cation **1** exhibited identical bond distances and angles. Interestingly, an intramolecular hydrogen bond was observed between the N3 and the O6 sites (N3H···O6): 2.7756(11) Å in **1**[NO_3], and 2.7798(11) Å in **1**[Cl]. This contact requires prior C5–C6 rotation and stabilizes the s-*cis* rotamer of **1** (Scheme 1). ^{1}H–^{1}H NOESY NMR experiments confirm that the s-*cis* conformation is maintained in solution (Fig. S14, SI). Separated treatment of **1**[NO_3] and **1**[Cl] with triethylorthoformate,[30,31] led to the formation of (s-*trans*) 1,3,7-trimethylhypoxanthinium nitrate, **2**[NO_3],[29] and chloride, **2**[Cl], respectively.

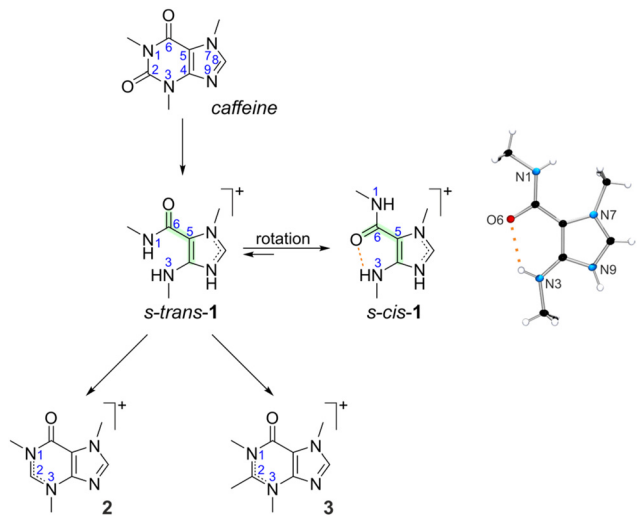

Scheme 1 Simplified synthetic routes towards cations **1**, **2**, and **3**. See SI for experimental details.

Interestingly, the C2(H) site in cation **2** exhibits certain acidic character, attributed to the electron-withdrawing effect of the adjacent methylated N1 and N3 positions, which facilitate deprotonation at this site.[32] Geometry of cation **2** remains within the expected parameters. In aqueous solution, the chloride salt crystallizes as monohydrate, **2**[Cl]·H_2O.[29]

The central focus of this study lies in the interplay of weak non-covalent interactions governing the crystal packing of **2**[Cl]·H_2O. These include conventional hydrogen bonds involving water molecules and halide anions, as well as anion···cation contacts *via* hydrogen bonding and n → π* interactions. While the latter interaction is a recurrent and structurally meaningful contact, our results indicate that it might not represent the most significant secondary stabilizing force. Geometrical parameters of the most relevant contacts are summarized in Table 1, and a complete description of hydrogen bonding interactions is provided in Table S1 (SI).

Within the crystal packing of **2**[Cl]·H_2O, a weak C2(H)···Cl1 hydrogen bonding contact of 3.4122(13) Å is observed. In addition, the chloride anion Cl1 forms hydrogen bonds with two symmetry-related water molecules, with O1w(H)···Cl1 separations of 3.2645(13) Å and 3.2701(13) Å (Fig. 1, left). These interactions suggest the coexistence and competition between electrostatic and orbital contributions.

Table 1 Selected intermolecular interactions [Å] involving cations **2** and **3**

	C2(H)···X[a]	H_2O···X[b]	X···C2[c]	X···plane[d]
2[NO_3]	3.081(12)	—	2.8265(16)	2.8253(13)
2[Cl]·H_2O	3.4122(13)	3.2645(13) 3.2701(13)	3.1744(12)	3.1767(8)
2[Br]·H_2O	3.5475(13)	3.4011(12) 3.4054(12)	3.2344(12)	3.2472(8)
2[I]	3.7312(18)	—	3.4859(19)	3.4888(11)
3[Cl]·3H_2O	—	3.0748(15) 3.0893(15)	3.1789(16)	3.1795(9)

X represents halogen or O atom, depending on the anion. [a] C···X distance in anion···cation H-bonding contacts. [b] O···X distance in cation···water H-bonding. X···C2 (n → π*) anion–cation contacts. [c] X···C interatomic distance (n → π* contact). [d] X···plane, distance from anion X to the nucleobase mean plane.

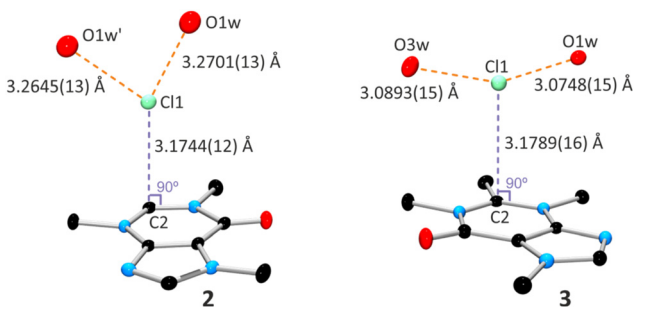

Fig. 1 Detail of the lone-pair → π* interaction and hydrogen bonding in **2**[Cl]·H_2O and **3**[Cl]·3H_2O.

More importantly, a supramolecular interaction caught our attention: the chloride anion (Cl1) in **2**[Cl]·H_2O is positioned directly above the C2 atom of the purine ring at a Cl1···C2 distance of 3.1744(12) Å (Fig. 1, left). This contact lies nearly perpendicular to the ring plane, as evidenced by the similar distance from Cl1 to the best hypoxanthinium plane (3.1767(8) Å). These values indicate that Cl1 is located along the axis perpendicular to the sp^2 orbitals at the C2 site instead of centered over the aromatic ring. Importantly, this Cl1···C2 distance is considerably shorter than both the Cl···H_2O hydrogen bonds present in the same structure (see Fig. 1, 3.2645(13) Å and 3.2701(13) Å), and the sum of the van der Waals radii for carbon and chlorine, 1.70 Å (C) + 1.75 Å (Cl) = 3.45 Å.[33] In other words, the short Cl1···C2 contact and the upright positioning of Cl1 are consistent with the presence of a strong n → π* interaction.

A similar arrangement is observed in **2**[NO_3], where an oxygen atom (O11) of the nitrate anion lies above the C2 atom at a distance of 2.8265(16) Å, with an essentially identical separation to the ring plane (2.8253(13) Å). These similar values confirm that O11 lies above the C2 site, thus supporting the existence of an analogous n → π* interaction involving the nitrate anion (Table 1).

To further investigate this n → π* interaction and assess whether it is preserved with other anions, it is reasonable to consider that the planar geometry of the nitrate anion does not rule out packing effects, as additional contacts may distort the nature of this interaction. Therefore, we synthesized the bromide and iodide salts of cation **2**, namely **2**[Br] and **2**[I] (see SI). Slow evaporation of aqueous solutions yielded single crystals of **2**[Br]·H_2O and **2**[I].[29]

The packing of **2**[Br]·H_2O was found to be isostructural with **2**[Cl]·H_2O, displaying a comparable arrangement in which Br1 lies directly above the C2 site at 3.2344(12) Å. This unsupported interaction is again remarkably shorter to that exhibited by both Br···H_2O hydrogen bonds, namely 3.4011(12) Å and 3.4054(12) Å (Table 1). Interestingly, while the halide···C2 distance increases slightly (+0.06 Å) compared to chloride, the hydrogen bonds involving Br are enlarged by approximately 0.14 Å, suggesting a stronger contribution of the n → π* interaction in the stabilization of the bromide salt.

In contrast, the iodide salt **2**[I] crystallizes without water molecules. Nevertheless, the iodide anion still adopts an upright orientation relative to the C2 site, with a contact distance of 3.4859(19) Å, and a similar distance to the best purine plane (3.4888(11) Å). The interaction sphere of iodide is completed by two hydrogen bonding contacts to C2(H) and C8(H) of neighboring cations **2**, at distances of 3.7312(18) Å, and 3.859(2) Å, respectively.

To explore the role of the C2 proton in the interaction, we synthesized a tetramethylated derivative of cation **2**, namely 1,2,3,7-tetramethylhypoxanthinium (**3**), where H2 is formally substituted by a methyl group. The subsequent chloride salt crystallizes in water as **3**[Cl]·3H_2O (Fig. 1, right),[29] and displays a comparable molecular geometry. Its crystal packing exhibits a well-defined hydrogen bonding pattern (Fig. S42, SI). Remarkably, the presence of a methyl group at the C2 site does not affect the positioning of the Cl^- anion, which maintains on top of the C2 site with a contact distance of 3.1789(16) Å, essentially identical to that in **2**[Cl]·H_2O. However, hydrogen bonding distances involving Cl1 and water molecules become shorter (3.0748(15) Å and 3.0893(15) Å, Fig. 1, right), indicating a redistribution of interaction strength. Thus, the lower electrophilic character of the C2(CH_3), compared to C2(H), diminishes the n → π* charge transfer in favor of hydrogen bonding.

Thus, consistent observation of short, directional halide···C2 contacts across all compounds, regardless of anion type, hydration state, or substitution, demonstrates the robustness and structural conservation of this n → π* interaction.

Hirshfeld surface and fingerprint analysis

This study aims to evaluate the halide···C2 n → π* interaction within the broader context of weak intermolecular forces that govern the crystal packing of these systems. Particular emphasis is placed on assessing its relative importance within the overall interaction hierarchy.

Initial insights can be derived from Hirshfeld surface analysis and the associated fingerprint plots. The Hirshfeld surface defines the region around a molecule in which its electron density dominates over that of neighboring molecules, and the fingerprint plots visualize the distribution and nature of intermolecular contacts across this surface. Fingerprint plots of **2**[Cl]·H_2O and **2**[Br]·H_2O were generated and analyzed using Crystal Explorer.[34] Both compounds exhibit similar patterns, those for **2**[Br]·H_2O, selected as the model system due to higher-quality diffraction data (see further discussion below), are depicted in Fig. 2. The plot for **2**[Cl]·H_2O is provided in the

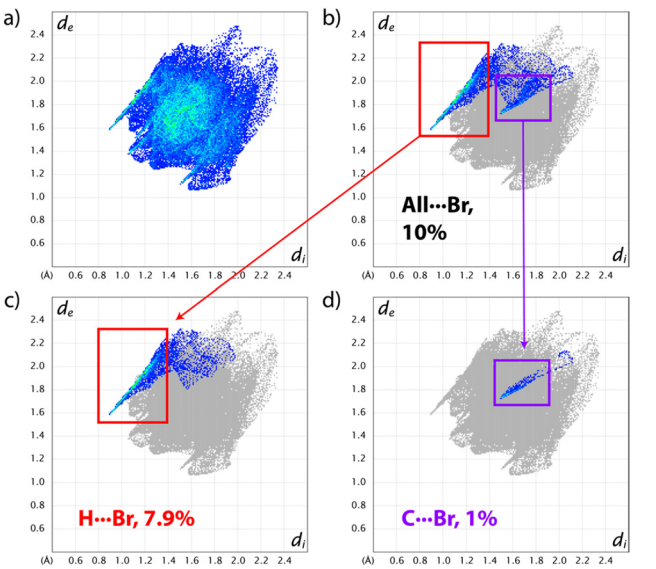

Fig. 2 Fingerprint plots for cation **2** in **2**[Br]·H_2O. (a) All intermolecular contacts; (b) contacts involving Br as the external (acceptor) atom; (c) H···Br contacts; (d) C···Br contacts. Colored markers and arrows are included as visual guides to correlate features across the subplots.

SI. The central region of the molecular surface shows the largest contribution, with sharp spikes appearing at low (d_i, d_e) values, indicative of close contacts. In 2[Br]·H_2O, interactions involving the bromide anion account for approximately 10% of the total surface area (Fig. 2b). A pronounced spike appears at (d_i, d_e) values of (0.9, 1.6), corresponding primarily to H···Br contacts, which constitute the dominant subset of halide interactions (7.9%), as shown in Fig. 2c. While Br···C2 contacts represent only 1% of the surface, Fig. 2d reveals that this small but non-negligible contribution matches to a secondary spike in the fingerprint plot, highlighting the presence of a directional halide···C2 interaction.

Experimental charge density and electrostatic mapping

A deeper understanding of the strength and nature of these intermolecular interactions was achieved through experimental charge density analysis based on high-resolution X-ray diffraction data of 2[Br]·H_2O, complemented by quantum chemical calculations on the crystal packing of the halogenated salts 2[Cl]·H_2O, 2[Br]·H_2O, 2[I], and 3[Cl]·$3H_2O$.

The Independent Atom Model (IAM) of 2[Br]·H_2O, obtained using Olex2,[35] served as the starting point for refining the asphericity of the electron density distribution. This refinement was conducted using multipolar refinement based on the Hansen–Coppens formalism,[36] implemented *via* the MoPro software suite.[37] Full details of the refinement procedure are provided in the SI. Intermolecular interactions were subsequently visualized and analyzed using MoProViewer.[38]

Analysis of the Laplacian distribution in the refined multipolar model of 2[Br]·H_2O (Fig. S48, SI) reveals a clear electron density depletion at the C2 position along the axis normal to the purine ring plane, precisely in the direction of the bromide anion. This anisotropic distribution correlates with a region of elevated electrostatic potential on the molecular surface at C2, as illustrated in Fig. 3a. Indeed, C2 is identified as the most electrophilic region of the cation, while the most nucleophilic region is located on the oxygen atom.

These experimental findings fully agree with our theoretical Molecular Electrostatic Potential (MEP) calculations. In cation 2 of 2[Cl]·H_2O, the most electrophilic region is localized along the extension of the C2–H bond, where $V_{s,max}$ reaches 124 kcal mol^{-1} (Fig. 3b). The region surrounding the C2 atom also displays large positive values in the MEP map (>100 kcal mol^{-1}), supporting its role as an anion-binding site. As mentioned above, the packing of 2[Cl]·H_2O exhibit short contacts between the chloride anion and both C2 and crystallization water molecules, with calculated penetration indices[19] of 22.8% (C2···Cl1) and 30.3% (O1w(H)···Cl1).

In parallel, the theoretical MEP of cation 3 (Fig. 3c) reveals that the electron density distribution on the six-membered ring remains largely similar to that of cation 2. However, the presence of a methyl group instead of hydrogen at the C2 site prevents the formation of hydrogen bonding, and slightly shifts the point of most positive potential towards the region between the C2–CH_3 and N1–CH_3 moieties. This shift results

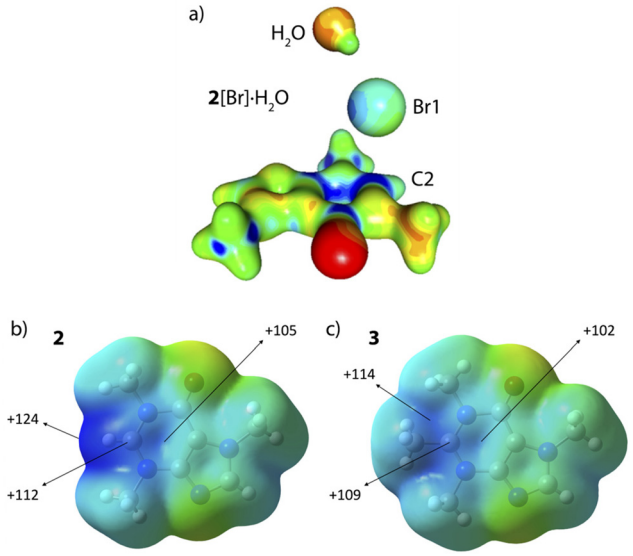

Fig. 3 Molecular electrostatic potential (MEP) mapped onto the 0.001 au electron density isosurfaces for (a) 2[Br]·H_2O derived from experimental multipolar refinement; (b) cation 2 in 2[Cl]·H_2O and (c) cation 3 in 3[Cl]·$3H_2O$ both calculated at the M06-2X/def2-TZVP level of theory. Energy values are given in kcal mol^{-1}.

in a lower $V_{s,max}$ value of 114 kcal mol^{-1} and corresponds to a lower penetration index of 22.3% for the C2···Cl1 contact.

QTAIM analysis of experimental electron density

To further probe the nature of this interaction, we performed a topological analysis of the experimental electron density of 2[Br]·H_2O using the Quantum Theory of Atoms in Molecules (QTAIM).[20] The analysis identified seven (3, −1) bond critical points (BCPs) involving the bromide anion, as shown in Fig. 4. The experimental results confirm the presence of a bond path between Br1 and C2, which, according to Bader's criteria, constitutes a necessary and sufficient condition for the existence of a bonding interaction.[20] This bond path is observed as a straight connection between the two atoms, contrasting with systems such as boron-centered triel bonds with chloride, in which no bond path was observed between the halide and the π-hole of the boron center.[39]

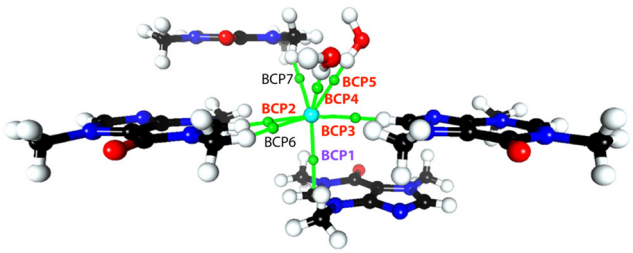

Fig. 4 Experimentally determined bond paths (green lines) between the Br^- anion and surrounding atoms in the crystal structure of 2[Br]·H_2O. Bond critical points (green spheres) are labeled according to their assignments in Table 2.

Main topological parameters associated with the bond critical points (BCP) are summarized in Table 2. The electron density at the bond critical point (ρ_{CP}) reflects the accumulation of electron density along the bond path, being its local minimum value along the bond path, and a local maximum in the other two directions. The Laplacian of the electron density ($\nabla^2\rho_{CP}$) indicates whether the electron density is concentrated ($\nabla^2\rho_{CP} < 0$, typical of covalent interactions) or depleted ($\nabla^2\rho_{CP} > 0$, characteristic of closed-shell interactions). The kinetic and potential (G_{CP} and V_{CP} respectively) energy densities,[40] represent the local contribution of electron motion, or electron–nucleus and electron–electron attractive interactions. Moreover, potential energy density is related to the strength of bonding and the attractive forces in the bond critical point. The potential energy density relates to bond strength, while the sign of H_{CP} (total energy density) provides insight into the interaction character: negative H_{CP} values typically indicate covalent interactions, whereas small positive values are consistent with closed-shell, non-covalent interactions. All seven reported BCPs identified in the crystal structure of **2**[Br]·H_2O show similar trends: small ρ_{CP}, positive $\nabla^2\rho_{CP}$, and positive and small H_{CP} values, characteristic of closed-shell interactions, consistent with the electrostatic nature of hydrogen bonds and Br···C interactions. Among them, the strongest topological values are found in CP4 and CP5, corresponding to Br···H_2O hydrogen bonds, together with CP2 (shorter C(H)···Br interaction), followed by CP1 (the Br···C2 n → π* interaction), CP3, and finally CP6 and CP7, which involve weaker Br···H (C_{methyl}) contacts.

It is noteworthy that the charge density and Laplacian values at the bond critical point associated with the n → π* interaction in **2**[Br]·H_2O (ρ = 0.078 e Å^{-3}, $\nabla^2\rho$ = 0.79 e Å^{-5}) are substantially higher than those reported for analogous contacts between iodide anions and quinoid rings (ρ = 0.0405 e Å^{-3}, $\nabla^2\rho$ = 0.42 e Å^{-5}; ρ = 0.0141 e Å^{-3}, $\nabla^2\rho$ = 0.15 e Å^{-5}).[7] This enhancement might be possibly due to the fact that this interaction is significantly more spatially confined in **2**[Br]·H_2O, where it involves a single sp^2 carbon atom (C2) rather than a more delocalized ring system involving multiple carbon atoms, as observed in earlier studies.

Table 2 Experimental topological properties of (3, −1) CPs in intermolecular interactions of **2**[Br]·H_2O: electron density [e Å^{-3}], Laplacian [e Å^{-5}], kinetic, potential and total energy density (G_{CP}, V_{CP}, H_{CP}; [kJ mol^{-1} Bohr^{-3}])

BCP		ρ_{CP}	$\nabla^2\rho_{CP}$	G_{CP}	V_{CP}	H_{CP}
1	Br1···C2	0.078	0.79	18.94	−16.18	2.76
2	Br1···H2	0.086	1.49	32.44	−24.15	8.29
3	Br1···H8	0.063	1.23	25.40	−17.40	8.00
4	Br1···H1W	0.084	1.30	28.81	−21.97	6.84
5	Br1···H2W	0.086	1.28	28.65	−22.27	6.38
6	Br1···H11[a]	0.043	0.64	13.23	−9.09	4.14
7	Br1···H13[a]	0.043	0.64	13.33	−9.20	4.13

[a] H11 and H13 are H atoms from methyl groups at N1 and N3, respectively.

These topological features indicate that topological parameters of the Br···C2 n → π* interaction are similar to conventional hydrogen bonds in terms of electron density characteristics. Therefore, their role in the crystal packing stabilization should not be ignored. This is particularly relevant considering that this interaction persists regardless of solvent content, or even in the absence of crystallization water.

Theoretical topological analysis and charge transfer

QTAIM analysis of the theoretical electron density derived from the crystal geometries (Table 3) confirms the presence of a bond path between the halide and the C2 atom in all studied compounds. Bond critical points exhibit electron densities (ρ) near 0.01 au and positive Laplacian values ($\nabla^2\rho$), both indicative of closed-shell interactions. Furthermore, total electronic energy density (H) values are positive and close to zero in all cases, further confirming the non-covalent, electrostatic character of these contacts. In addition, delocalization indices (DI) between the halide and C2 suggest a small, but non-negligible, transfer of electron density.

The agreement between experimental and theoretical topological parameters for the Br···C2 interaction (Tables 2 and 3) further supports its structural relevance. This consistency reinforces the validity of both experimental and theoretical approaches and provides a solid basis for extending the analysis to other halide salts in the series, including those with varying hydration content.

We then shifted our focus to the nature and electronic features of the X···C2 contacts. Geometrically, this interaction is highly favorable, with halide···carbon penetration values ranging from 19.2% to 23.2%, and approach angles close to

Table 3 Computed QTAIM parameters at the DFT level for halide···C2 interactions in the solid-state geometries of **2**[Cl]·H_2O, **2**[Br]·H_2O, **2**[I] and **3**[Cl]·H_2O. Electron density [e Å^{-3}], Laplacian [e Å^{-5}], kinetic, potential and total energy density (G, V, H; [kJ mol^{-1} Bohr^{-3}])

Adduct	ρ	$\nabla^2\rho$	G	V	H	DI(X,C)
2[Cl]·H_2O	0.080	0.747	18.12	−15.75	2.37	0.073
2[Br]·H_2O	0.087	0.723	18.38	−17.07	1.31	0.085
2[I]	0.073	0.554	14.18	−13.13	1.05	0.074
3[Cl]·3H_2O	0.078	0.771	18.12	−15.49	2.63	0.056

Table 4 Main geometrical features, BSSE-corrected interaction energies and NBO second-order perturbation energies for the adducts **2**[Cl]·H_2O, **2**[Br]·H_2O, **2**[I] and **3**[Cl]·H_2O in their crystal structures geometries. All energies are given in kcal mol^{-1}[a]

Adduct	$p_{C\cdots X^-}$ (%)	α^a (°)[a]	ΔE_{int}	$E^{(2)}$ $n_{X^-} \rightarrow \pi^*_{C-N}$
2[Cl]·H_2O	22.8	87.3	−92.3	4.73
2[Br]·H_2O	23.2	91.4	−90.5	5.99
2[I]	19.2	92.6	−84.5	4.19
3[Cl]·3H_2O	22.3	88.3	−91.4	3.55

[a] Angle α: H2–C2···X.

90°, suggesting a well-aligned overlap (Table 4). This directionality, combined with proximity, supports a dominant halide···C2 interaction over alternative contacts with the nucleobase. Interaction energies are substantial, as expected for ionic pairs, and consistent with previous reports of halides interacting with large cations.[41]

The Natural Bond Orbital (NBO) analysis reveals that the primary charge transfer process involves the delocalization of a halide lone pair into an empty antibonding π^*_{C-N} orbital (Fig. 5). The associated second-order perturbation energies, $E^{(2)}$, range from 3.55 to 5.99 kcal mol^{-1}, confirming the relevance of this n → π* interaction.

To further complete our study, we performed full geometry optimizations of the halide adducts. Compound **2**[Br]·H_2O was selected as a representative case due to its strong interaction (as seen in Table 3). Upon optimization, the Br···C2 separation significantly decreased, yielding a penetration of 75.5%, compared to 23.2% in the crystal structure. This was accompanied by a loss of planarity in the N1–C2(H)–N3 moiety, indicating that while the sum of the three angles at C2 is 360° in the crystal structure, it drops to 349° in the optimized structure, indicating a shift toward sp^3 hybridization. Such behavior has been previously observed in other systems displaying n → π* interactions.[6,42,43]

Interestingly, this structural deformation is not observed in the solid-state crystal. A plausible explanation is that, within the crystal packing, the bromide anion is involved in additional interactions, most notably, hydrogen bonds with two water molecules (penetration values of 41.7% and 43.6%), and weaker contacts with methyl groups (penetration range: 3.8%–28.8%), as illustrated in Fig. 4 (see also SI). These interactions, particularly those involving protic hydrogen donors, likely reduce the electron-donating capacity of the bromide anion, preventing the full charge transfer to C2. In fact, when the geometry optimization is repeated with the two crystallization water molecules included, the Br1···C2 penetration is only 41.9%, and the N1–C2(H)–N3 angles nearly recover planarity (sum of angles = 359.8°). Therefore, the presence of all these electron density attractors around the halide seems to be essential for establishing the n → π* interaction with the C2 atom of the hypoxanthinium ring without further change in the hybridization of the latter.

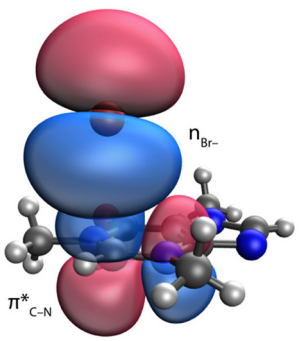

Fig. 5 Donor (Br^- lone pair) and acceptor (π^*_{C-N}) NBO orbitals involved in the main charge transfer process in **2**[Br]·H_2O.

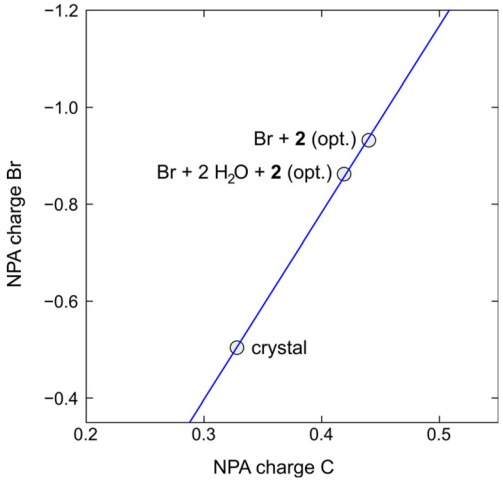

Fig. 6 Correlation between the C2 and Br1 atomic charges in the different systems studied.

Further insight comes from Natural Population Analysis (NPA) charges. The atomic charge of bromine becomes more negative when the system is simplified to include only Br1 and the nucleobase cation, while it is less negative in full crystal geometry. Conversely, the C2 atom shows higher positive charge in the isolated model and becomes less electropositive in the crystal environment. These trends indicate that both charge transfer and coulombic attraction are attenuated in the presence of surrounding electron-withdrawing interactions. Remarkably, a strong linear correlation (R^2 = 0.999) exists between the NPA charges of Br1 and C2 across all computational models studied (Fig. 6).

Conclusions

In this work, we report and characterize a novel n → π* interaction in a series of halide-hypoxanthinium systems displaying strengths comparable to conventional hydrogen bonds. To understand the nature and significance of this interaction, we performed a combined experimental and theoretical approach based on high-resolution charge density analysis and quantum chemical calculations.

Experimental quantum crystallography of **2**[Br]·H_2O reveals a well-defined bond path between the bromide anion and the C2 carbon atom, namely the most electrophilic site in the purine ring, as confirmed by molecular electrostatic potential (MEP) maps. The corresponding bond critical point exhibit topological features characteristic of closed-shell interactions, with electron density and Laplacian values that exceed those reported for more delocalized anion···π systems, and approach those observed for hydrogen bonds.

Our theoretical analysis further confirms the localized nature of this halide···C2 interaction, elucidating its geometry, energy profile, and charge redistribution. Notably, Natural Bond Orbital (NBO) analysis reveals significant charge delocalization from the halide lone pair into the antibonding π^*_{C-N}

orbital of the nucleobase. Theoretical models also allowed us to explore the effect of structural substitutions and solvation on the interaction strength, revealing that crystal packing and secondary interactions moderate the charge transfer efficiency and hybridization of the C2 center.

The strong agreement between experimental and computational results provides a coherent description of this n → π* non-covalent interaction. Our findings expand the understanding of directional supramolecular forces, which may play important roles in molecular recognition and crystal engineering.

Conflicts of interest

There are no conflicts to declare.

Data availability

The datasets supporting this article have been uploaded as part of the supplementary information (SI). Supplementary information: experimental details, NMR measurements, calculations and X-ray diffraction data, and quantum crystallography. See DOI: https://doi.org/10.1039/d5dt02386f.

CCDC 2475635 (for **1**[NO_3]), 2475636 (for **1**[Cl]), 2475637 (for **2**[NO_3]), 2475638 (for **2**[Cl]·H_2O), 2475639 (for **2**[Br]·H_2O), 2475640 (for **2**[I]), 2475641 (for **3**[Cl]·$3H_2O$), and 2475642 (for high resolution **2**[Br]·H_2O) contain the supplementary crystallographic data for this paper.[29a–h]

Acknowledgements

Financial support from the University of Zaragoza, the Aragón Government (A. P. predoctoral fellow, E42_23R, E05_23R), and the MCIU/AEI/FEDER (PID2021-122406NB-I00) is kindly acknowledged. P. G. O. thanks Prof. Benoît Guillot, Nancy, for helpful comments regarding the MoProViewer tool.

References

1 M. Egli and R. V. Gessner, *Proc. Natl. Acad. Sci. U. S. A.*, 1995, **92**, 180–184.
2 M. L. DeRider, S. J. Wilkens, M. J. Waddell, L. E. Bretscher, F. Weinhold, R. T. Raines and J. L. Markley, *J. Am. Chem. Soc.*, 2002, **124**, 2497–2505.
3 B. C. Gorske, B. L. Bastian, G. D. Geske and H. E. Blackwell, *J. Am. Chem. Soc.*, 2007, **129**, 8928–8929.
4 S. K. Singh and A. Das, *Phys. Chem. Chem. Phys.*, 2015, **17**, 9596–9612.
5 T. J. Mooibroek, P. Gamez and J. Reedijk, *CrystEngComm*, 2008, **10**, 1501–1515.
6 R. W. Newberry and R. T. Raines, *Acc. Chem. Res.*, 2017, **50**, 1838–1846.
7 V. Milašinović, V. Vuković, A. Krawczuk, K. Molčanov, C. Hennig and M. Bodensteiner, *IUCrJ*, 2023, **10**, 156–163.
8 S. K. Singh, K. K. Mishra, N. Sharma and A. Das, *Angew. Chem., Int. Ed.*, 2016, **55**, 7801–7805.
9 J. Echeverría, J. D. Velásquez and S. Alvarez, *Cryst. Growth Des.*, 2020, **20**, 7180–7187.
10 J. Echeverría, *Cryst. Growth Des.*, 2018, **18**, 506–512.
11 D. Quiñonero, C. Garau, C. Rotger, A. Frontera, P. Ballester, A. Costa and P. M. Deyà, *Angew. Chem., Int. Ed.*, 2002, **41**, 3389–3392.
12 B. P. Hay and R. Custelcean, *Cryst. Growth Des.*, 2009, **9**, 2539–2545.
13 H. T. Chifotides and K. R. Dunbar, *Acc. Chem. Res.*, 2013, **46**, 894–906.
14 D. X. Wang and M. X. Wang, *Acc. Chem. Res.*, 2020, **53**, 1364.
15 Y. Zhao, Y. Cotelle, L. Liu, J. López-Andarias, A. B. Bornhof, M. Akamatsu, N. Sakai and S. Matile, *Acc. Chem. Res.*, 2018, **51**, 2255.
16 X. Lucas, A. Bauzá, A. Frontera and D. Quiñonero, *Chem. Sci.*, 2016, **7**, 1038–1050.
17 A. Frontera, P. Gámez, M. Mascal, T. J. Mooibroek and J. Reedijk, *Angew. Chem., Int. Ed.*, 2011, **50**, 9564–9583.
18 S. Alvarez, *Dalton Trans.*, 2013, **42**, 8617–8636.
19 J. Echeverría and S. Alvarez, *Chem. Sci.*, 2023, **14**, 11647–11688.
20 R. F. W. Bader, *Atoms in Molecules – A Quantum Theory*, Oxford University Press, Oxford, 1990.
21 M. Egli and S. Sarkhel, *Acc. Chem. Res.*, 2007, **40**, 197–205.
22 H. Biltz and H. Rakett, *Ber. Dtsch. Chem. Ges.*, 1928, **61**, 1409–1422.
23 R. M. Hoskinson, *Aust. J. Chem.*, 1968, **21**, 1913–1919.
24 Bruker AXS Inc., *SADABS, Area Detector Absorption Program*, Bruker AXS Inc., Madison, WI, USA, 1996.
25 L. Krause, R. Herbst-Irmer, G. M. Sheldrick and D. Stalke, *J. Appl. Crystallogr.*, 2015, **48**, 3–10.
26 G. M. Sheldrick, *Acta Crystallogr., Sect. A:Found. Crystallogr.*, 2008, **64**, 112–122.
27 G. M. Sheldrick, *Acta Crystallogr., Sect. C:Struct. Chem.*, 2015, **71**, 3–8.
28 L. J. Farrugia, *J. Appl. Crystallogr.*, 2012, **45**, 849–854.
29 (*a*) CCDC 2475635: Experimental Crystal Structure Determination, 2025, DOI: 10.5517/ccdc.csd.cc2p3364; (*b*) CCDC 2475636: Experimental Crystal Structure Determination, 2025, DOI: 10.5517/ccdc.csd.cc2p3375; (*c*) CCDC 2475637: Experimental Crystal Structure Determination, 2025, DOI: 10.5517/ccdc.csd.cc2p3386; (*d*) CCDC 2475638: Experimental Crystal Structure Determination, 2025, DOI: 10.5517/ccdc.csd.cc2p3397; (*e*) CCDC 2475639: Experimental Crystal Structure Determination, 2025, DOI: 10.5517/ccdc.csd.cc2p33b8; (*f*) CCDC 2475640: Experimental Crystal Structure Determination, 2025, DOI: 10.5517/ccdc.csd.cc2p33c9; (*g*) CCDC 2475641: Experimental Crystal Structure Determination, 2025, DOI: 10.5517/ccdc.csd.cc2p33db; (*h*) CCDC 2475642: Experimental Crystal Structure Determination, 2025, DOI: 10.5517/ccdc.csd.cc2p33fc.

30 R. Walentowski and H.-W. Wanzlick, *Chem. Ber.*, 1969, **102**, 3000–3005.
31 F. Eßer, Dissertation, Technische Universität Berlin, 1964. For our preparation, see SI.
32 A. Makhloufi, W. Frank and C. Ganter, *Organometallics*, 2012, **31**, 7272–7277.
33 A. Bondi, *J. Phys. Chem.*, 1964, **68**, 441–451.
34 M. A. Spackman and J. J. McKinnon, *CrystEngComm*, 2002, **4**, 378–392.
35 O. V. Dolomanov, L. J. Bourhis, R. J. Gildea, J. A. K. Howard and H. Puschmann, *J. Appl. Crystallogr.*, 2009, **42**, 339–341.
36 N. K. Hansen and P. Coppens, *Acta Crystallogr., Sect. A: Found. Crystallogr.*, 1978, **34**, 909–921.
37 C. Jelsch, B. Guillot, A. Lagoutte and A. Lecomte, *J. Appl. Crystallogr.*, 2005, **38**, 38–54.
38 B. Guillot, E. Enrique, L. Huder and C. Jelsch, *Acta Crystallogr., Sect. A:Found. Adv.*, 2014, **70**, C279.
39 C. Escudero-Adán, A. Bauzá, C. Lecomte, A. Frontera and P. Ballester, *Phys. Chem. Chem. Phys.*, 2018, **20**, 24192–24200.
40 E. Espinosa, E. Molins and C. Lecomte, *Chem. Phys. Lett.*, 1998, **285**, 170–173.
41 D. M. Gil, J. Echeverría and S. Álvarez, *Inorg. Chem.*, 2022, **61**, 9082–9095.
42 J. Echeverría, *Chem. Commun.*, 2018, **54**, 3061–3064.
43 J. Echeverría, *Inorg. Chem.*, 2018, **57**, 5429–5437.